Copper Segregation to the ∑5 (310)/[001] Symmetric Tilt Grain Boundary in Aluminum

Geoffrey H. Campbell, Jürgen M. Plitzko,* Wayne E. King
Chemistry and Materials Science Directorate, University of California, Lawrence Livermore National Laboratory, Livermore, CA 94550, USA

Stephen M. Foiles
Materials and Process Modeling Dept., Sandia National Laboratories, Albuquerque, NM 87185 USA

Christian Kisielowski
National Center for Electron Microscopy, Ernest Orlando Lawrence Berkeley National Laboratory, University of California, Berkeley, CA, 94550, USA

Gerd J. M. Duscher
Material Science and Engineering Dept., North Carolina State University, Raleigh, NC 27695, USA and Solid State Physics Department, Oak Ridge National Laboratory, Oak Ridge, TN 37831, USA

**Current address: Max Planck Institute for Biochemistry, Department of Molecular and Structural Biology, Martinsried, Bavaria, Germany*

Prepared for submission to a special volume of Interface Science carrying the proceedings of the Euroconference on "Structure and Composition of Interfaces in Solids", held August 18 – 23, 2002 at Kloster Irsee, Irsee, Germany

Abstract

New insight into the atomic segregation of copper to an aluminum grain boundary has been obtained using multiple, complementary atomic resolution electron microscopy techniques coupled with ab-initio electronic structure calculations. The copper segregation is site specific and changes the structure of the boundary by occupying interstitial sites. Minor elemental constituents in materials can have profound effects on their engineering performance. This change in structure can be associated with these strong effects. The observed structural change will alter the mass transport behavior of the boundary and has implications for the understanding of electromigration mechanisms.

1. Introduction

It has long been appreciated that segregation of minor constituents to grain boundaries (GBs) can have considerable impact on the properties and performance of engineering materials. The earliest work was performed on metals with respect to their mechanical properties, especially in low alloy steels, and the review by Westbrook [1] is an excellent overview of this work. Of course, segregation is also important for ceramics [2] and electronic materials, such as the important role of Cu in Al interconnects for microelectronics [3] in increasing their resistance to failure induced by electromigration.

Evidence for the segregation of minor species to GBs was indirect in the earliest studies. The observation of absolute surface and GB energies by zero creep experiments as a function of metal impurity content was a usual approach [4, 5]. The advent of Auger electron spectroscopy [6] allowed for a direct measure of GB segregation [7, 8], provided a means for inducing intergranular fracture was available. The use of analytical electron microscopy (AEM) [9] allows for the compositional analysis of intact GBs [10], especially since the introduction of commonly available field emission electron sources that allow for nanometer sized analysis volumes in the specimen [11]. Another powerful method that has been applied to GB and interface segregation is atom probe field ion microscopy [12], which has atomic scale resolution of structure and composition. A limited number of high–resolution transmission electron microscopy (HREM) investigations of segregation have been performed, notably on Bi segregation to Cu GBs [13, 14].

Modeling of segregation to GBs has followed thermodynamic [15] and atomistic approaches [16]. The thermodynamic approaches have often followed analogous derivations as for surface adsorption [17]. Examples are the modification by McLean [18] of the Langmuir [19, 20] adsorption isotherm, the modification by Seah and Hondros [21] of the Brunauer, Emmett, and Teller (BET) theory [22, 23], and the modification by Hondros and Seah [17] of the Fowler isotherm [24].

We have approached the modeling of GB segregation with atomistic simulation methods incorporating electronic structure calculations. The simulations place constraints on the types of GBs that can be considered, e.g. they must be periodic and have reasonably small repeat units. Experimentally, we have fabricated the identical GB as considered in the simulation as a macroscopic bicrystal. We performed HREM with complimentary transmission electron microscopy (TEM) based techniques, including focal series reconstruction [25] and Z-contrast imaging [26], and compared the observations with the predictions of the simulations. While copper in solution within aluminum normally resides at substitutional sites on the Al lattice, we report here the discovery of copper atoms occupying interstitial positions at this GB.

2. Methods

Both the modeling and the experimental investigations of GB place constraints on the type of boundary that can be investigated. The limits tend to push the boundary character towards high symmetry special boundaries. The modeling requires that small numbers of atoms be considered in the simulation

ensemble and that periodic boundary conditions can be drawn on the structure. The experimental approaches used here require low index directions of the crystals on either side of the GB be contained in the GB plane such that the crystal lattice can be imaged in the TEM. These considerations have guided us to study the $\sum 5$ (310)/[001] symmetric tilt grain boundary (STGB) in the face-centered cubic system.

2.1. Modeling

Previous investigations of the $\sum 5$ (310)/[001] STGB in the Al-Cu system [27-29] have considered structures predicted by embedded atom method (EAM) potentials using conjugate gradient relaxations in molecular statics. We have extended those calculations here by employing *ab-initio* electronic structure calculations in the local density approximation of density functional theory using a plane wave basis and ultrasoft pseudopotentials as implemented in the VASP code [30]. These calculations should provide greater predictability and reliability compared to the earlier calculations. The calculations are performed in a periodically repeated cell which contains two oppositely oriented grain boundaries. The number of planes separating the grain boundaries was varied and the results were found to be largely insensitive for the size of cell used. In the [001] direction, the periodic repeat length was always chosen to be one lattice constant. Thus the calculations actually represent the addition or modification of fully occupied columns along the tilt axis. The segregation energies were computed by comparing the energy of the system with the Cu atoms located at the boundary with the energy of the system with the Cu atom located in the bulk region between the boundaries.

2.2. Experiments

The experimental approach was to fabricate the same GB at the macroscale as a bicrystal and characterize the GB structure by HREM techniques in order to compare to the predictions of the theory.

2.2.1. Grain Boundary Fabrication

The bicrystal was fabricated by ultra-high vacuum diffusion bonding [31] of precisely oriented single crystals. The single crystals were made of an alloy composition of 1 at.% Cu balance Al by the Bridgeman technique. The Cu was kept in solid solution after growth from the melt by homogenizing in the single phase field followed by rapid cooling. The crystal was oriented and cut in 3 mm slices with the faces parallel to (310). Specially developed lapping procedures [32] were used to prepare flat and highly polished surfaces parallel to (310) to within 0.1°. The crystals were mutually misoriented by a 180° rotation about the (310) surface normals and a reference flat was placed on the sides of the crystals in order to re-establish the orientation prior to diffusion bonding.

After introduction of the oriented single crystals into the UHV environment of the diffusion bonding machine, they are cleaned by sputtering with 1 keV Xe at a glancing angle of 15° while being rotated. Sputtering is effective at removing the oxide surface layer which forms when Al is exposed to air. The oxygen partial pressure within the UHV environment is low enough that the sputtered surface remains free of an oxide layer for many hours. In this condition the Al surfaces, if touched together, would bond together instantly at room temperature. Therefore, the mutual twist orientation of the crystals must be re-established with (310) surfaces close together, but not touching. When the crystals are properly oriented, then the faces are carefully brought into contact, a small load is applied to keep the assembly together, and heat was provided to bring the bicrystal to 540°C. It was held at this temperature for 8 h to allow diffusion to eliminate void space and create a dense interface. To establish a more nearly equilibrium condition for the interface, the bicrystal was held at 200°C for 100 h in a separate Ar atmosphere furnace and rapidly cooled in air.

2.2.2. Transmission Electron Microscopy

Specimens were made by electropolishing followed by low-angle, low-energy ion milling, which has been shown to create high quality TEM specimens [33, 34]. The AEM was performed with X-ray energy dispersive spectroscopy (EDS) analysis on a VG-HB501 dedicated STEM and the electron spectroscopic imaging (ESI) was performed with a Zeiss EM912 TEM equipped with an in-column Ω energy filter. The high resolution TEM was performed on a Philips CM300-FEG Ultra-twin (the One Ångström Microscope [33, 35]) at the National Center for Electron Microscopy at Lawrence Berkeley National Laboratory. The Z-contrast imaging was performed on the VG-HB603-U dedicated STEM at Oak Ridge National Lab.

The acquisition of a through focal series suitable for exit wavefunction reconstruction is only possible through computer control of the microscope. A series of 20 to 40 images with equally spaced focus values were typically acquired for this study. Drift correction is critical for accurate focal series reconstruction. The only effective way found in this study to correct for the drift was by manual post processing of the individual images in a focal series. The focal series reconstruction was performed with the Philips software [36, 37] developed as part of the Brite-Eurem project [38].

2.3 Exit Surface Wavefunction Simulation

To investigate the form of the exit electron wavefunction as a function of the parameters of specimen thickness, extent of segregation, and atomic structure, simulations were performed with the EMS suit of simulation tools [39]. The wavefunction produced from the simulation of an electron plane wave traversing the specimen is complex. To view the results, one typically chooses to represent it as an amplitude image and a phase image. The phase image was found to be most sensitive to the elemental composition of the atomic columns in the image and was therefore used in this study.

2.4 Distortion correction for Z-contrast images

The Z-contrast image acquisition is a serial technique, where the electron beam is rastered across the specimen and the signal from the detector is synchronously recorded. The acquisition time is on the order of 5 to 10 seconds. During this time, instrument instabilities such as specimen drift, vibration, or stray electromagnetic fields will couple with scan coil miscalibration to produce distortions in the final image. The first order distortions due to the constant velocity component of drift or scan coil miscalibration have been removed by image processing [40]. Higher order distortions due to, for example, accelerations from oscillations of the specimen have not been removed.

3. Results

3.1. Modeling

In the first phase of the modeling, the structure for the ∑5 (310)/[001] STGB was simulated using EAM potentials. This structure was then optimized using the electronic structure calculations. Since it is known that Cu resides as a substitutional impurity, various sites in the model were individually switched from Al occupancy to Cu and the structure was again relaxed using the electronic structure calculations. In addition, various structures with two or three Cu atoms per CSL cell were also considered. The energy change for each configuration was then calculated specifically for each of the candidate sites for Cu segregation. The energetics indicate that there is a strong segregation energy (0.46 eV) to one of the sites on the central plane and that there is also a similar driving force to provide partial occupation of sites in the two adjacent planes. These sites are summarized in Figure 1A.

After the initial experimental results were available, it became obvious that interstitial sites needed to be considered in the simulations. One interstitial site in particular, symmetrically located in the GB plane and of a comparatively large size turned out to be very energetically favorable as a result of the simulation. In fact, this site was found to be more energetically favorable that any of the substitutional sites with a segregation energy of 0.65 eV. The results of the simulations including interstitial sites are shown in Figure 1B.

3.2. Transmission Electron Microscopy

3.2.1. Analytical Electron Microscopy

The AEM results using EDS and ESI were consistent with one another. The results of the EDS are shown in Figure 2, which shows the counts from Cu recorded as a fine probe is stepped across the ∑5 (310)/[001] STGB. The image calculated from ESI analysis is shown in Figure 3. The Cu L_3 absorption edge is used with the three window technique [41] to form the image.

3.2.2. Phase Contrast with Exit Surface Wavefunction Reconstruction

The ∑5 (310)/[001] STGB was imaged along the common [001] tilt axis in the HREM and a focal series of 30 images was acquired from a focus value of –148 nm to –79 nm with a step size of 2.3 nm. These values were determined by Thon ring analysis [42] of the individual images and analysis of the intensity variation in two orthogonal {200} components of the Fourier transform of the images. From the comparison of individual images from the series with high-resolution image simulations, the thickness of the specimen was estimated to be 6 nm. However, this type of thickness estimation is well known to be inaccurate and to err on the side of being too thin [43]. The phase image calculated from the reconstructed exit surface wavefunction is shown in Figure 4. Distortion correction was performed on this image; however, the corrections were so small as to be negligible.

Immediately evident is appreciable intensity in the phase image at the position of the interstitial site. Since phase shift is directly related to crystal potential, we can conclude that the interstitial site is occupied.

3.2.3. Z-Contrast Imaging

The same specimen that was used for the exit wavefunction reconstruction was then used for Z-contrast imaging, with only a brief low-angle, low-energy ion-milling step to clean the specimen in between. The Z-contrast image acquired is shown in Figure 5A. Considerable noise in the image is evident arising from stray electro-magnetic fields. These stray fields were unusual for the particular installation and it is thought that they were arising from a faulty area light outside of the building. A low-pass filter in Fourier space can remove the high frequency noise in the image due to these stray fields. The frequency cut-off for the filter was placed at approximately 20 nm^{-1}, well beyond the information limit of the microscope. The probe size for this instrument is 0.12 nm at FWHM, which leads to a resolution limit of the same scale. The results of the filtering step are shown in Figure 5B.

Distortion correction was performed on this image and considerable distortions were found. In particular, differing magnifications in the x- and y- directions of 8% were found. A shear correction of about 2° was also needed to bring the image of the perfect crystal regions on either side of the GB into a 4-fold symmetric structure.

3.3 Exit Surface Wavefunction Simulation

The atomic model of the GB with Cu segregation predicted by atomistic simulation was used as the input for the simulation of the exit plane wavefunction. The thickness of the specimen in the simulation was chosen to be 6.5 nm, close to the estimated specimen thickness. The results of the simulation are shown in Figure 6A, where the phase image has been calculated. Comparison of this simulation with the experimental image in Figure 6B shows obvious differences, firstly in the intensity of the signal from the interstitial site and secondly in the separation of the intensities from the atomic columns. A possible explanation for the difference in phase shift at the interstitial site is less than 100% filling of the site with Cu. The overall resolution of the atomic columns appears also to be degraded over what was assumed in the simulation for Fig. 6A. Since the microscope used for this study has been demonstrated to possess an information limit of less than 0.1 nm [44], the origin of this resolution degradation requires further investigation. A simulation is shown in Figure 6C that includes only 50% filled interstitial sites with the resolution of the image degraded by a low-pass filter in Fourier space placed at 0.14 nm. With these parameters used in the simulation, a better match to the experimental data is found.

4. Discussion

4.1. Grain Boundary Structure

The focal series reconstruction of the exit surface wavefunction did not show great chemical sensitivity in this case. The effect on the magnitudes of the calculated phase image at the position of the copper atoms residing in the interstitial sites of the GB was quite subtle. The phase shift measured here was less than what was observed at the position of a column of Al atoms in the perfect crystals portions of the image. A less than fully filled column on interstitial sites would explain the low level of phase shift, however this result is inconsistent with a rough estimation of the percentage of sites filled based on the calculated segregation energy, which is very close to 100%. The degradation in resolution due to misalignment of the individual images in the focal series and modulation transfer function of the detector, as discussed earlier, could contribute to the low level of phase shift observed, but whether these factors explain all of the effect is speculative at this point.

The Z-contrast imaging of the GB clearly shows high intensity signal at a specific periodic position in the GB. However, clearly associating that high intensity position with the interstitial site requires additional analysis of the image. The distortions present in the image as acquired were too large to unambiguously align it with the atomic model. During the alignment procedure it becomes obvious that the perfect crystal regions of the Z-contrast image do not overlay these regions of the model, i.e. the perfect crystal areas of the crystal aligned along [001] do not appear cubic. If we make the assumption that the perfect crystal areas must be cubic, then distorting the image to reproduce the required symmetry removes much of the distortions present in the image. These distortions appear to be inherent to the Z–contrast technique due to the serial nature of the data acquisition. Over the time span of several seconds required to raster the beam over the target area of the specimen, instabilities in the instrument will induce distortions in the image. When they are removed, however, the match with the atomic model and the reconstructed phase image becomes very good. At this stage it becomes clear cut that the high intensity regions arising from elemental species of a greater atomic number than the Al matrix are arising from the positions of the interstitial site of the GB. The results of the AEM prove that this high Z species is, in fact, Cu. The combined data from the focal series reconstruction of the exit wavefunction, the Z–contrast imaging, and the atomistic simulations are shown in Fig. 7.

4.2. Implications for Grain Boundary Properties

We find that the Cu atoms assume interstitial sites at this Al GB. This structure is quite stable and diffusion of Cu is considered to be more difficult than if the Cu was substitutional. Likewise, the presence of Cu is expected to influence Al and vacancy diffusion at the GB. For the related case of self-diffusion of Cu in the $\sum 5$ (310)/[001] symmetric tilt GB, the mechanisms of self-diffusion have been reported in detail [45]. This study by atomistic simulation indicated that the dominant diffusion mechanism for the elemental boundary involved an interstitialcy mechanism involving the interstitial site identified here. One would expect the behavior of the elemental Al boundary to be qualitatively similar to that observed for Cu due to their common crystal structure. The occupation of the interstitial site by the impurity will thus modify the diffusion behavior of the boundary. In particular, it should shut off the dominant diffusion mechanism for the elemental version of this boundary and so retard diffusion. Since structural holes are expected to be a common feature of grain boundaries, one would expect that the segregation of a smaller impurity, such as Cu in Al, will frequently fill those locations in other GBs as well. This structural change of the GB will remove potential interstitial based diffusion mechanisms and so retard GB diffusion. This picture provides a detailed mechanistic understanding of the role that Cu additions to Al may play in the enhanced resistance of Al-Cu alloys to electromigration.

5. Conclusions

We conclude that the combination of atomistic theory with two complementary approaches to high-resolution electron microscopy and analytical microscopy techniques to the characterization of a model boundary provides important information on site-specific segregation of Cu to Al grain boundaries. However, even with current electron microscope resolution, we are limited to observing only a handful of special grain boundaries with short repeat unit periodic structures. For the foreseeable future, information on more general boundaries will come from theory that has been benchmarked by comparison with these special boundaries. It appears that this approach offers the possibility to extend this study to other grain boundaries, which could add substantially to the understanding of grain boundary controlled properties in materials.

Acknowledgements

We thank Prof. M. Rühle for access to specimen preparation facilities and analytical electron microscopes at the Max-Planck-Institut für Metallforschung in Stuttgart. We thank the National Center for Electron Microscopy at Lawrence Berkeley National Lab for use of their facilities for both specimen preparation and HREM. We thank Oak Ridge National Lab for the use of VG-HB603-U for Z-contrast imaging. This work performed under the auspices of the U. S. Department of Energy, Office of Basic Energy Sciences by the University of California, Lawrence Livermore National Laboratory under Contract No. W-7405-Eng-48.

References

1. J.H. Westbrook, Metall. Rev. **9,** 415 (1964).
2. W.D. Kingery, in Ceramic Microstructures '86 Role of Interfaces, edited by J.A. Pask and A.G. Evans (Plenum Press, New York, 1986), p. 281.
3. R. Rosenberg, J. Vac. Sci. Technol. **9,** 263 (1972).
4. E.D. Hondros, Proc. Roy. Soc. A **286,** 479 (1965).
5. M.C. Inman and H.R. Tipler, Metall. Rev. **8,** 105 (1963).
6. D. Briggs and M.P. Seah, *Practical Surface Analysis* (Wiley, New York, NY, 1990).
7. E.D. Hondros and M.P. Seah, Scripta Metall. **6,** 1007 (1972).
8. M.P. Seah and E.D. Hondros, Proc. Roy. Soc. A **335,** 191 (1973).
9. E. Bischoff, G.H. Campbell and M. Rühle, Fresenius J. Anal. Chem. **337,** 469 (1990).
10. P. Doig and P.E.J. Flewitt, Acta Metall. **29,** 1831 (1981).
11. J.S. Vetrano, E.P. Simonen and S.M. Bruemmer, Acta Mater. **47,** 4125 (1999).
12. B.W. Krakauer and D.N. Seidman, Rev. Sci. Instrum. **63,** 4071 (1992).
13. U. Alber, H. Mullejans and M. Rühle, Acta Mater. **47,** 4047 (1999).
14. D.E. Luzzi, M. Yan, M. Sob and V. VÌtek, Phys. Rev. Lett. **67,** 1894 (1991).
15. S. Hofmann, in Surface Segregation Phenomena, edited by P.A. Dowben and A. Miller (CRC Press, Boca Raton, FL, 1990), p. 107.
16. S.M. Foiles, in Surface Segregation Phenomena, edited by P.A. Dowben and A. Miller (CRC Press, Boca Raton, FL, 1990), p. 79.
17. E.D. Hondros and M.P. Seah, Metall. Trans. A **8,** 1363 (1977).
18. D. McLean, *Grain Boundaries in Metals* (Clarendon Press, Oxford, 1957).
19. I. Langmuir, J. Am. Chem. Soc. **37,** 1139 (1915).
20. I. Langmuir, J. Am. Chem. Soc. **40,** 1361 (1918).
21. M.P. Seah and E.D. Hondros, Scripta Metall. **7,** 735 (1973).
22. S. Brunauer, P.H. Emmett and E. Teller, J. Am. Chem. Soc. **60,** 309 (1938).
23. S. Brunauer, L. Deming, W.E. Deming and E. Teller, J. Am. Chem. Soc. **62,** 1723 (1940).
24. R.H. Fowler and E.A. Guggenheim, *Statistical Thermodynamics* (Cambridge University Press, Cambridge, 1939).
25. E.J. Kirkland, Ultramicroscopy **15,** 151 (1984).
26. S.J. Pennycook, S.D. Berger and R.J. Culbertson, J. Microsc.– Oxford **144,** 229 (1986).
27. X.Y. Liu, W. Xu, S.M. Foiles and J.B. Adams, App. Phys. Lett. **72,** 1578 (1998).
28. C.L. Liu, X.Y. Liu and L.J. Borucki, Acta Mater. **47,** 3227 (1999).
29. C.L. Liu, X.Y. Liu and L.J. Borucki, App. Phys. Lett. **74,** 34 (1999).
30. G. Kresse and J. Firthmüller, Phys. Rev. B **54,** 11169 (1996).
31. W.E. King, G.H. Campbell, A.W. Coombs, G.W. Johnson, B.E. Kelly, T.C. Reitz, S.L. Stoner, W.L. Wien and D.M. Wilson, in Joining and Adhesion of Advanced Inorganic Materials, edited by A.H. Carim, D.S. Schwartz and R.S. Silberglitt (Materials Research Society, Pittsburgh, PA, 1993), p. 61.
32. W.L. Wien, G.H. Campbell and W.E. King, in Microstructural Science, edited by D.W. Stevens, E.A. Clark, D.C. Zipperian and E.D. Albrecht (ASM International, Materials Park, OH, 1996), p. 213.
33. C. Kisielowski, C.J.D. Hetherington, Y.C. Wang, R. Kilaas, M.A. O'Keefe and A. Thust, Ultramicroscopy **89,** 243 (2001).
34. A. Strecker, J. Mayer, B. Baretzky, U. Eigenthaler, T. Gemming, R. Schweinfest and M. Rühle, J. Microsc. – Oxford **48,** 235 (1999).

35. M.A. O'Keefe, C.J.D. Hetherington, Y.C. Wang, E.C. Nelson, J.H. Turner, C. Kisielowski, J.-O. Malm, R. Mueller, J. Ringnalda, M. Pam and A. Thust, Ultramicroscopy **4,** 215 (2001).
36. W.M.J. Coene, A. Thust, M. deBeeck and D. VanDyck, Ultramicroscopy **64,** 109 (1996).
37. A. Thust, M. Lentzen and K. Urban, Ultramicroscopy **53,** 101 (1994).
38. D. Van Dyck, H. Lichte and K.D. van der Mast, Ultramicroscopy **64,** 1 (1996).
39. P.A. Stadelmann, Ultramicroscopy **21,** 131 (1987).
40. G.H. Campbell, D. Cohen and W.E. King, Microsc. Microanal. **3,** 299 (1997).
41. J.M. Plitzko and J. Mayer, Ultramicroscopy **78,** 207 (1999).
42. F. Thon, Z. Naturforsch. **20a,** 154 (1965).
43. M. O'Keefe and V. Radmilovic, in Proceedings XIIIth International Congress for Electron Microscopy, edited by B. Jouffrey, et al. (Editions de physique, Les Ulis, 1994), p. 361.
44. A. Ziegler, C. Kisielowski and R.O. Ritchie, Acta Mater. **50,** 565 (2002).
45. M.R. Sørensen, Y. Mishin and A.F. Voter, Phys. Rev. B **62,** 3658 (2000).

Figure Captions

Figure 1 – Ball model representations of the predictions for the atomic structure of the ∑5 (310)/[001] STGB in Al with Cu segregation from atomistic simulations. The Al atoms are shown as grey while the Cu atoms are red. (A) When only substitutional positions are considered, the possible positions for Cu segregation are shown. The dark red site has a segregation energy of 0.46 eV. The light red sites are expected to be approximated half occupied with a segregation energy of 0.46 eV up to half occupancy but reducing for higher occupancy. (B) When the interstitial sites are considered, one has substantial segregation energy of 0.65 eV. The two Cu atoms represented in the figure reside at equivalent interstitial sites.

Figure 2 – (A) The X-ray energy dispersive spectra from a small electron probe (approximately 0.2 nm FWHM) placed on the GB and slightly off the GB. The heights of the peaks in the spectra have been adjusted such that the aluminum peaks are equal. The increase in Cu signal at the GB is seen by the increase in peak height. (B) Standardless quantification gives a qualitative indication of the Cu content in the volume probed by the electron spot. The increase in Cu signal at the GB as the beam is stepped across is seen to be greater than the counting errors in the peak integration.

Figure 3 – (A) The bright field TEM image from the area analyzed showing the position of the GB. (B) The electron spectroscopic image formed with the signal from the Cu L_3 absorption edge. The slight enhancement in the signal running in a line where the GB is located in the bright field image shows the Cu segregation to the GB. The white rectangle indicates the area from which the data are integrated to form the plot. (C) Plot of the horizontally integrated signal in the boxed region shows an increase in counts from Cu at the GB.

Figure 4 – The phase image determined from the focal series reconstruction of the exit surface wavefunction for the ∑5 (310)/[001] STGB in Al-1at.% Cu alloy. An arrow in the image indicates the position of the interstitial site that exhibits appreciable signal.

Figure 5 – The Z-contrast image acquired from the same ∑5 (310)/[001] STGB as imaged in Fig. 2. (A) The image as-acquired with substantial noise arising from stray fields. (B) The Fourier filtered image with the noise removed. Image distortions are also removed. The periodic bright spots at the boundary plane coincide with the position of the interstitial site in the GB.

Figure 6 – (A) The phase part of the simulated exit surface wavefunction for the ∑5 (310)/[001] STGB using the structure predicted in Fig. 1B for a thickness of 6.5 nm. (B) The experimentally derived phase image from focal series reconstruction. (C) The phase part of the simulated exit surface wavefunction for similar conditions as in (A), however now with Cu occupancy reduced to 50% and microscope information limit degraded to 1.4 nm.

Figure 7 – A composite image combining the data acquired in this study. The alignment of the z-contrast image with the phase image of the reconstructed exit wavefunction and the atomic model from atomistic simulation clearly show the signal arising from the interstitial site in the GB.

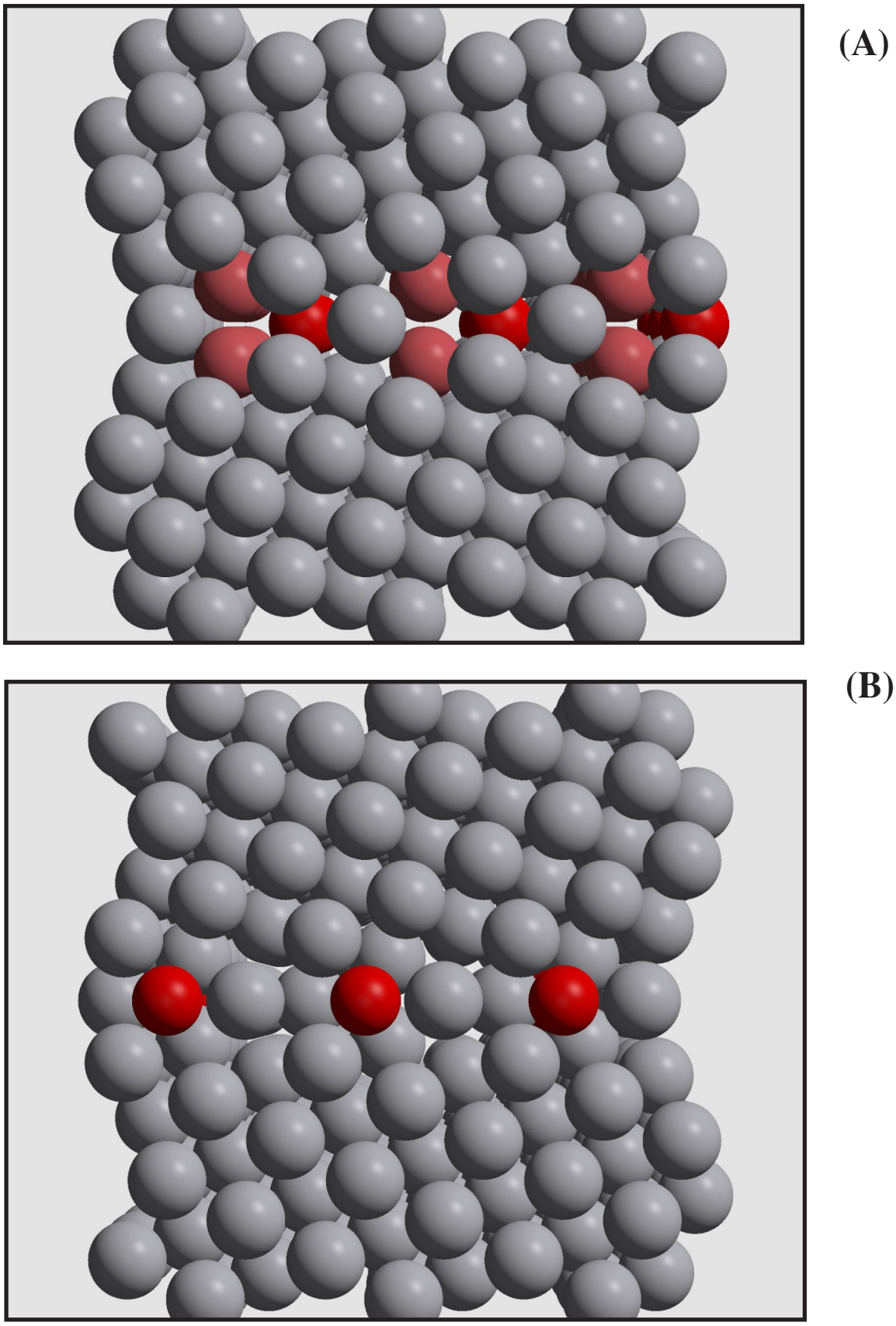

Figure 1

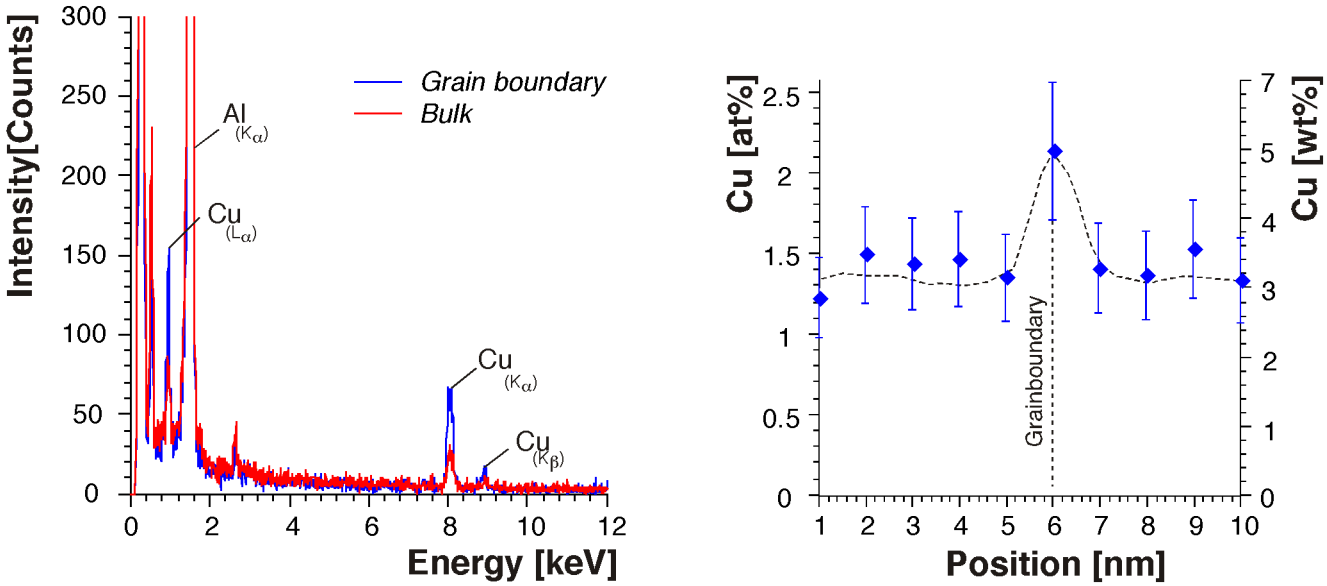
Intensity[Counts]
Energy [keV]
Grain boundary
Bulk
Al (Kα)
Cu (Lα)
Cu (Kα)
Cu (Kβ)
Cu [at%]
Cu [wt%]
Position [nm]
Grainboundary

(A) **(B)**

Figure 2

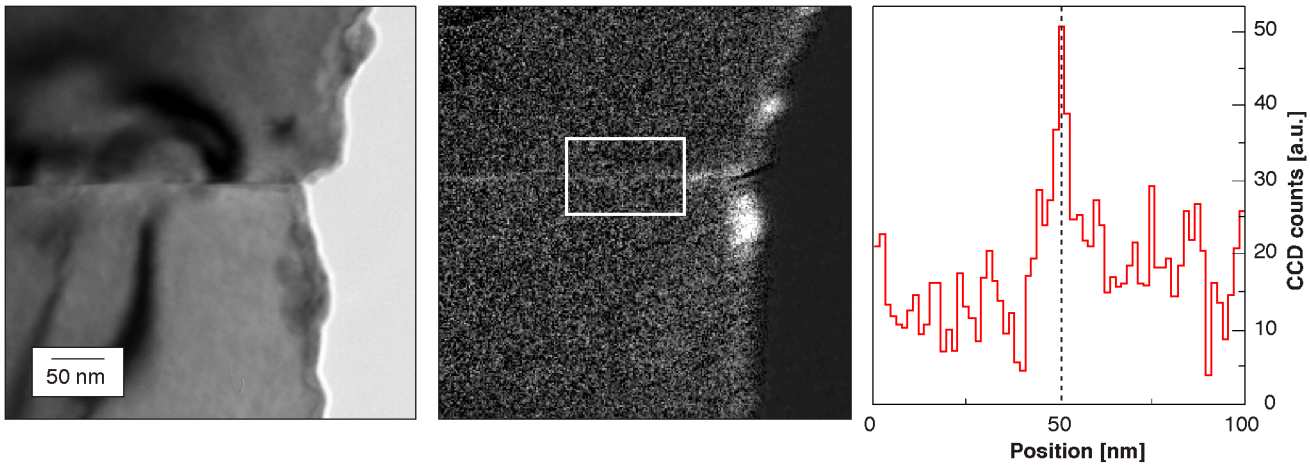

(A) **(B)** **(C)**

Figure 3

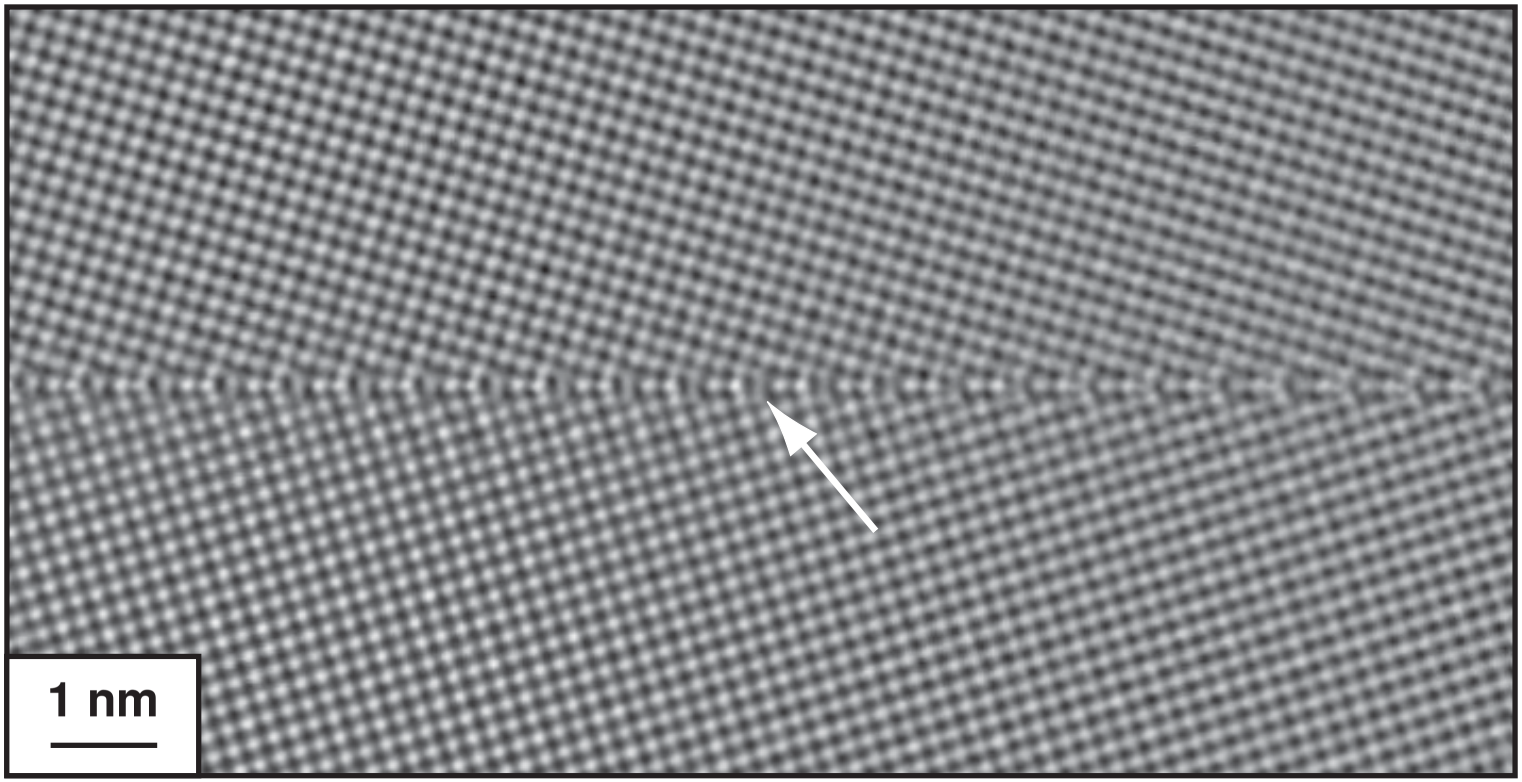

Figure 4

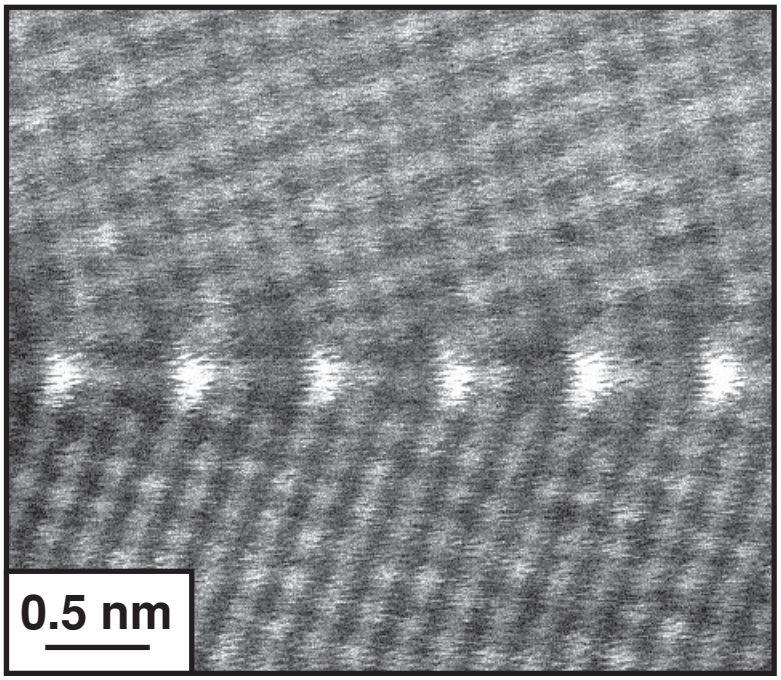

(A)

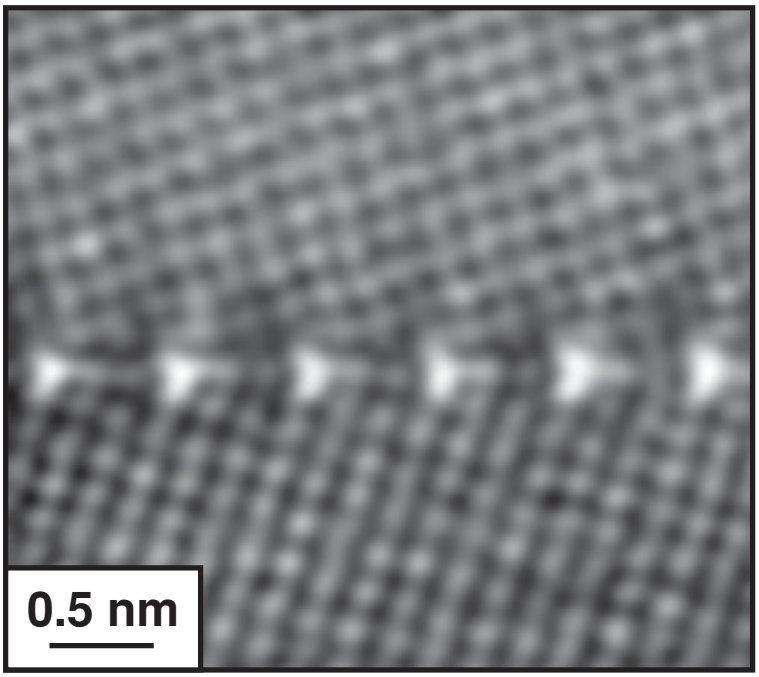

(B)

Figure 5

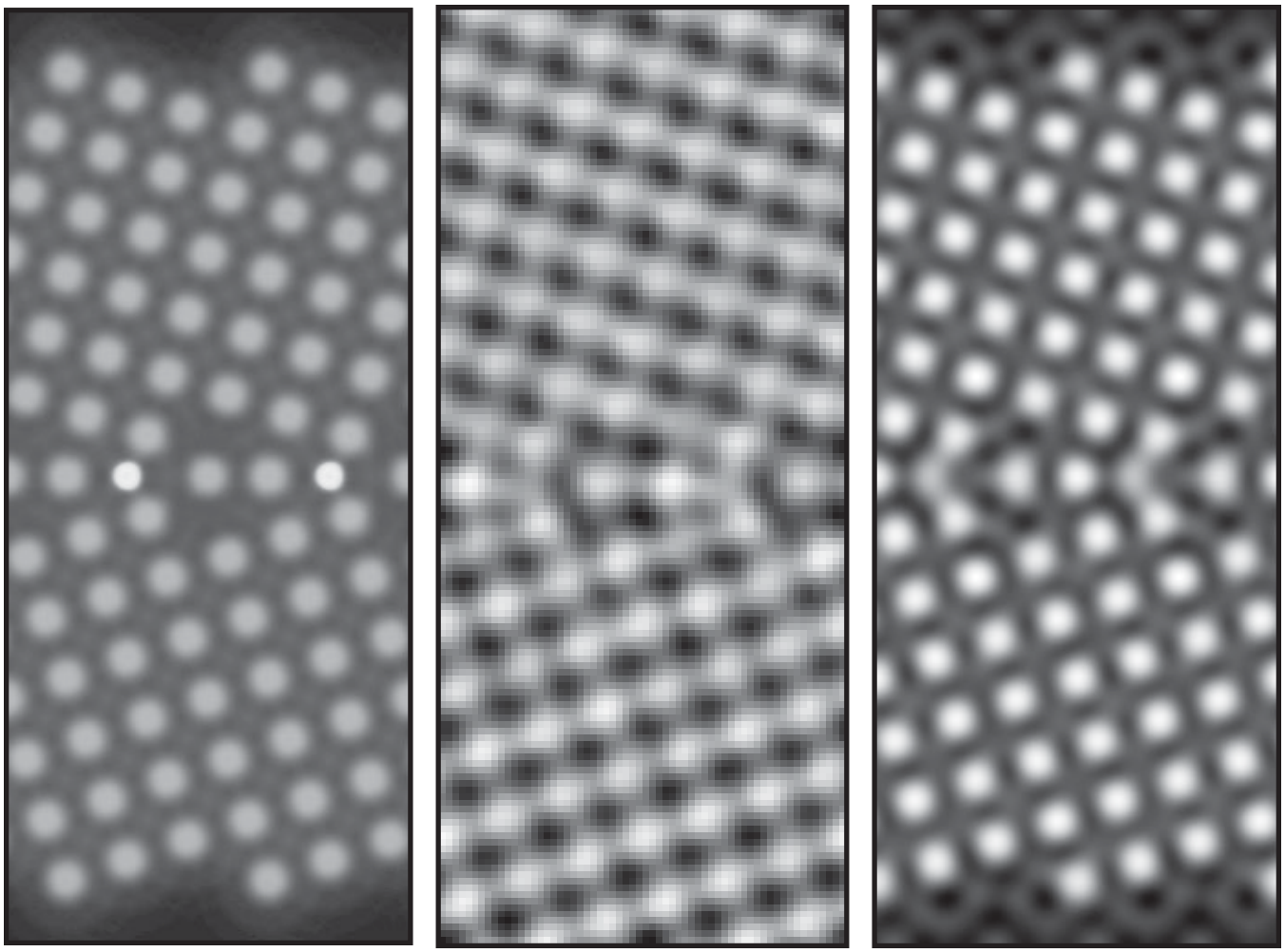

(A) **(B)** **(C)**

Figure 6

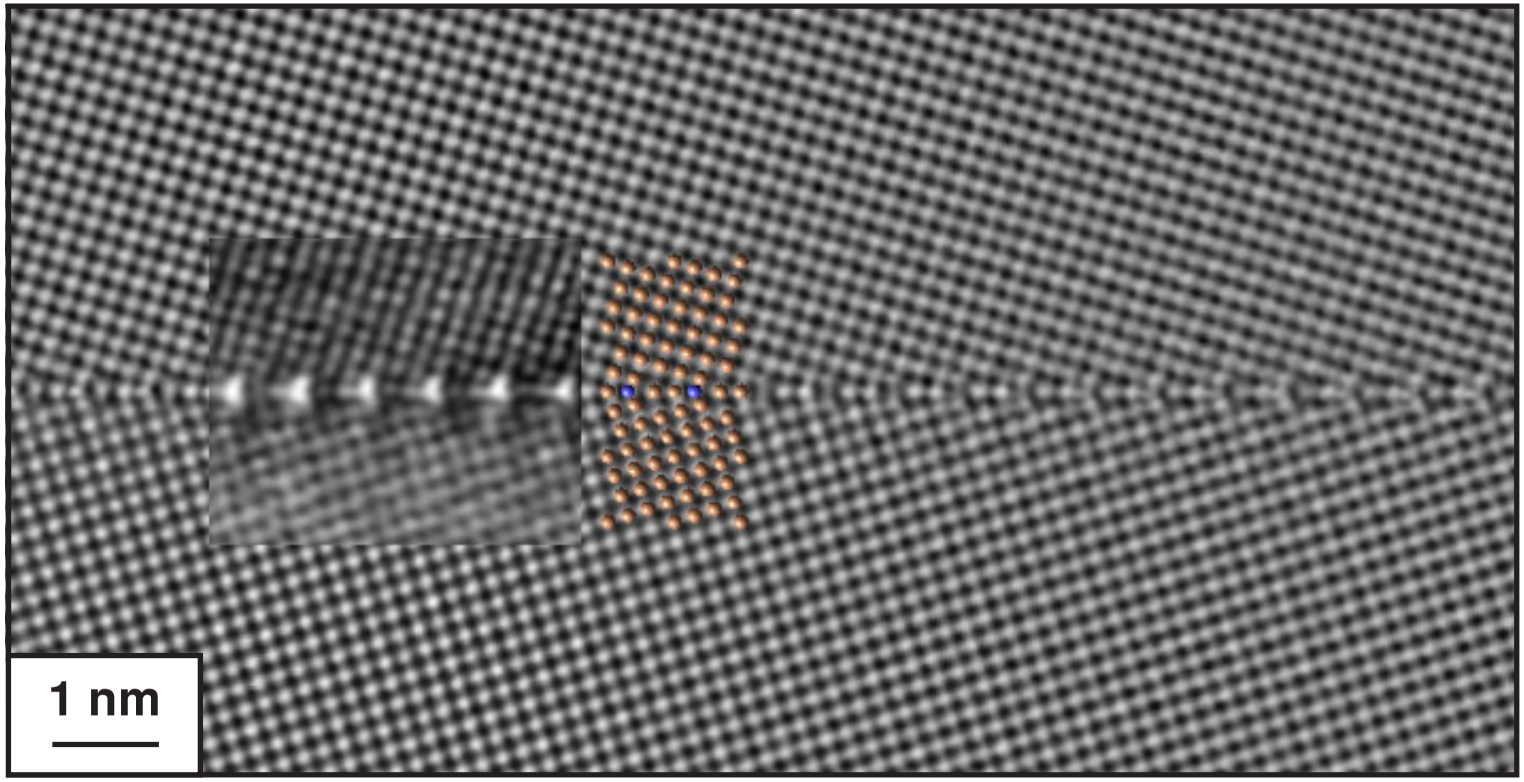

Figure 7